The characteristics of galaxies with powerful radio jets

Zheng, X.

5 Radio-loud AGN jet alignment
Radio and Optical Position Angle of Radio Galaxies

Xuechen Zhang, Yuze Zhang, Huub Röttgering

(Submitted to A&A)

Abstract

It is well established that active galactic nuclei (AGNs) play an important role in the evolution of galaxies. These AGNs can be linked to the accretion processes onto massive black holes and past merger events in their host galaxies, which might lead to the alignment of the jets with respect to the host galaxies. This paper presents a study of the position angle (PA) differences between radio and optical images of radio AGNs based on the second data release (DR2) of the Low Frequency Array (LOFAR) Two-Meter Sky Survey (LoTSS), the *Karl G. Jansky* Very Large Array First Images of the Radio Sky at Twenty-Centimeters Survey (FIRST), the Dark Energy Spectroscopic Instrument (DESI) Legacy Imaging Surveys and the Sloan Digital Sky Survey (SDSS). We assessed PA measurement biases in the data and classified the radio AGNs based on the radio luminosity and infrared colour from the Wide-field Infrared Survey Explorer (WISE). This resulted in a radio AGN sample with reliable radio and optical PA measurements. The PA difference (dPA) distributions for the radio AGN samples show a prominent minor-axis alignment tendency. We simulated the projection effect to estimate the intrinsic jet-galaxy alignment based on some simple assumptions. The observed dPA distribution can be well described by a two-component jet-alignment model, which consists of a component being more aligned with the minor axis of the host galaxy and the other being less aligned. The fitting results indicate that the jet alignment is dependent on radio luminosity and the shape of galaxies, with the jets being more likely to be aligned with the minor-axis of the galaxy for lower

luminosity and elongated radio AGNs. The minor-axis alignment of the entire sample may suggest a coherent model of accretion present in most AGN host galaxies, while a considerable number of bright radio-AGN with massive host galaxies might have undergone a chaotic model of accretion or past merger events.

5.1 Introduction

It has been known for a long time that active galactic nuclei (AGN) play an important role in the evolution of their host galaxies (Shankar et al. 2009). These AGN are the result of the accretion process of the super-massive black holes (SMBHs) at the centre of galaxies. Multiple evidence has shown that an increase in inflow leads to the prevalence of AGN activity (e.g. Best et al. 2005b; Dunn & Fabian 2006; Best et al. 2007). AGN release considerable energy into the surrounding galactic medium and the inter-galactic medium (IGM; Boehringer et al. 1993b). The energy released by AGN takes two different forms; radiation and mechanical energy (Best & Heckman 2012). The energy output has been related to the classification of AGN, by comparing it with the corresponding accretion rate at the Eddington limit (Eddington rate; Best & Heckman 2012). Radiation is dominant for high excitation AGN, which is a type of radiative mode AGN with strong high-ionization narrow lines (Best & Heckman 2012). These sources, along with the rest of the radiative mode AGN population, are products of efficient accretion at a rate above 1 per cent of the corresponding Eddington rate. The mechanical energy of ejected particles is dominant for low-excitation AGN with weak narrow low-excitation emission lines, which results from a lower accretion rate (Hine & Longair 1979; Laing et al. 1994). Regardless of the form, the energy outflow could potentially disrupt the inflow of gas and cease the AGN activity.

AGN jets from radio observations provide a probe of the accretion of SMBHs. There might be two ways of inflow in the central region of host galaxies; the coherent model and the chaotic model (Lagos et al. 2011). The coherent model is based on angular momentum preservation of the inflow, while in the chaotic model, there are shifts in angular momentum throughout the inflow process (Lagos et al. 2011). Revealed by previous simulation results, different inflow mechanisms result in different SMBH spin alignments and, therefore, radio-AGN jet directions (Hopkins et al. 2012; Lagos et al. 2011). Under conservation of angular momentum, jets from AGN accompanied by a coherent model of accretion are mostly perpendicular to their host galaxies' galactic plane. By contrast, jets from AGN with a chaotic model of accretion are randomly orientated with respect to their host galaxies. On top of these accretion models, an AGN jet might indicate possible merger events. During a merger event between two

galaxies, in which the spin of SMBHs can change significantly (Elmegreen et al. 2008; Bournaud et al. 2011). Also, the resulting AGN jet orientation is expected to be different after the merger.

Despite the dichotomy of these simulation results, the two models as well as possible merger events suggest a link between AGN jet orientations and the accretion process. This relationship can be studied by comparing the radio and optical counterparts of the same source. An earlier observation-based study targeting the overall galactic population was conducted by Battye & Browne (2009) using data from the VLA First Images of the Radio Sky at Twenty-Centimeters Survey (FIRST; Becker et al. 1995) and the Sloan Digital Sky Survey (SDSS; York et al. 2000) to study the alignment between radio and optical images of galaxies. Their radio-loud sub-sample does not provide a picture of AGN jet alignment with respect to their hosts, given the sample is contaminated by star-forming (SF) galaxies with the bulk of radio emissions from star formation inside the galactic plane. The random orientations shown in their radio-loud sub-sample can be interpreted as a sign of complex kinematics presented in a rounder and most massive galaxies (Emsellem et al. 2007), which might infer a decoupled core linked to the chaotic model. Also, for AGN with host galaxies having older stellar populations, no alignment tendency was observed. However, this might be due to a small sample size. Moreover, the projection effect, the discrepancy between intrinsic alignment and apparent alignment, was mentioned as another possible cause that might hide intrinsic alignment information.

In this paper, we present an analysis of the alignment between optical and radio images of radio AGNs and their sub-samples, along with simulations which demonstrate the link between the observation and intrinsic radio jet alignment with respect to their host galaxies. The primary goal of this study is to provide a further understanding of the accretion process for radio-loud AGN and their triggering/fueling mechanisms.

In this work, we mainly use the data from Low Frequecy Array (LOFAR) Two-metre Sky Survey (LoTSS; Shimwell et al. 2022). LOFAR reaches more than an order of magnitude deeper than the FIRST survey for sources with a typical spectral index (van Haarlem et al. 2013). The survey also has higher sensitivity to extended radio structures (Sabater et al. 2019). Hence, it is ideal for observing radio jet morphology during this research. The remaining sections of this paper are as follows. We first describe the data and data reduction process in Sect. 5.2. In Sect. 5.3,

the result of the alignment distribution of the overall sample and subsamples based on different divisions is presented. Next, in Sect. 5.4, we showcase the simulation results which link the apparent alignment result from observation to the intrinsic alignment of AGN jets. Finally, in Sect. 5.5, we discuss various physical implications of our observation and simulation results. Throughout this paper, we adopt a cosmology with the following relevant parameters: $\mathrm{H}_0 = 70 \mathrm{kms}^{-1}\mathrm{Mpc}^{-1}$, $\Omega_\mathrm{m} = 0.3$, $\Omega_\Lambda = 0.7$.

5.2 Data and sample

5.2.1 Surveys

Our radio sample is firstly selected from the LoTSS DR2 (Shimwell et al. 2022). The LoTSS project aims to observe the entire northern hemisphere in the frequency band 120-168 MHz using LOFAR. The LoTSS DR2 covered 27% of the northern sky (5634 square degrees) with an rms noise level of $83\,\mu\mathrm{Jy\,beam}^{-1}$ and a resolution of 6″. The area of coverage of LoTSS DR2 is the combination of two contiguous regions centred at RA $\sim$ 13h and RA $\sim$ 1h respectively. A total of 4 396 228 radio sources were detected in the Stokes I maps. The point-source completeness of this survey was about 90% at a peak brightness of $0.8\,\mathrm{mJy\,beam}^{-1}$ and the positional accuracy was about 0.2″.

In the LoTSS DR2, the source detection process was performed by using the Python Blob Detector and Source Finder (PyBDSF; Mohan & Rafferty 2015) on the mosaic images. PyBDSF uses wavelet decomposition to find high signal-to-noise (S/N) peaks in the images and fits them with one or more Gaussian components. These Gaussian components were grouped automatically to form radio sources in the LoTSS DR2 source catalogue. This process could detect and associate small sources ($\lesssim 15''$) with simple structures in the LoTSS DR2. The PyBDSF results would provide the deconvolved size and positional angle for the small and simple radio sources, contributing to the estimation of the jet alignment in the following analyses. The association of larger sources was processed by the Radio Galaxy Zoo (LOFAR) Zooniverse project[1].

The optical data used in the cross-matching process was based on the Dark Energy Spectroscopic Instrument (DESI) Legacy Imaging Surveys (hereafter the Legacy Surveys). The Legacy Surveys were a combination

[1] `https://www.zooniverse.org/projects/chrismrp/radio-galaxy-zoo-lofar`

of three public projects, the Dark Energy Camera Legacy Survey, the Beijing-Arizona Sky Survey and the Mayall z-band Legacy Survey, using three telescopes: the Blanco telescope at the Cerro Tololo Inter-American Observatory; the Mayall Telescope at the Kitt Peak National Observatory; and the University of Arizona Steward Observatory 2.3 m (90 inches) Bart Bok Telescope at Kitt Peak National Observatory. A total of 14 000 square degrees of extragalactic sky in the northern hemisphere was observed in the grz bands with uniform depths ($\sim$23 AB magnitude at r band). The point-spread functions (PSFs) in the Legacy Survey have a median full width at half maximum (FWHM) of about 1″, comparable to that for the SDSS images (Abazajian et al. 2009). The software package *Tractor* (Lang et al. 2016) was used to extract sources from the stack images and construct the source catalogue with morphological information, including the shapes and profiles of the galaxies. Based on this optically detected catalogue, the Legacy Surveys also provided mid-infrared magnitudes for each source in four bands (3.4, 4.6, 12 and 22 μm, also known as W1, W2, W3 and W4 bands) using the stack images from the Wide-field Infrared Survey Explorer (WISE Wright et al. 2010; Cutri et al. 2013; Mainzer et al. 2014).

The PyBDSF catalogue was refined and cross-matched with optical/infrared data following the procedures similar to Williams et al. (2019) to construct the value-added-catalogue (VAC) for the LoTSS DR2 (Hardcastle et al., in prep). The cross-matching procedures combined the likelihood ratio (LR) cross-matching method (e.g. Sutherland & Saunders 1992) and visual inspections. For each isolated and small radio source, the probability of a nearby optical object (candidate) being its counterpart would be estimated based on the position, brightness and colours of the object. This probability would be compared with the probability of the optical object being a random interloper, resulting in the LR of the optical source. The optical counterparts for the radio sources would be the candidate with the largest LR unless the LR was below a defined threshold. For the large radio sources, the Gaussian component associations and the optical counterpart identifications would be done by human eyes in the LOFAR Radio Galaxy Zoo involving a massive effort of many volunteers. Based on the cross-matching procedures, about 70% of the radio sources detected in the LoTSS DR2 have an optical counterpart in the Legacy Surveys. The detail photometry and photometric redshifts were produced by methods described in Kondapally et al. (2021) and Duncan et al. (2021). The

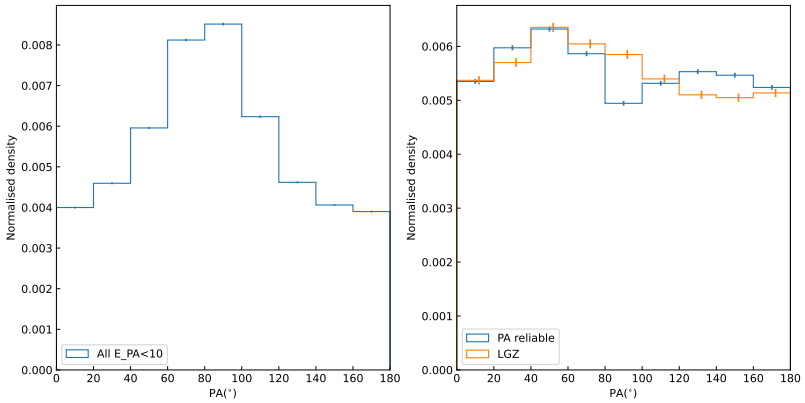

Figure 5.1: Normalised distribution of RPAs in bins of 20° for the radio sources in the LoTSS DR2. The panel on the left shows the distribution of RPAs of radio sources in the LoTSS DR2 with PA errors smaller than 10 degrees. The panel on the right shows the distribution of RPAs of the large multiple-Gaussian sources and the large LGZ sources. The blue histogram shows the RPA distribution of the multiple-Gaussian sources with reliable RPA and the red histogram shows the distribution of the large LGZ sources. The two histograms are normalised to make the area of integration to be one.

sources in this work are all selected from these radio sources with an optical counterpart.

5.2.2 Sample selection

To study the jet alignment within the galaxies, it is important to have reliable positional angle (PA) measurements in both optical and radio bands. In this section, we describe the bias and uncertainties in the measured radio PA (RPA) and optical PA (OPA) in the data, and the criteria we use to select a sample with reliable PAs.

RPA in the LoTSS DR2

The RPA in the LoTSS DR2 VAC was estimated in different ways depending on the source type (Williams et al. 2019). The RPA of radio sources with only one Gaussian component ('S_Code'='S' in the VAC) were defined

by the major axis of the Gaussian component. For radio sources fitted by multiple Gaussian components in PyBDSF and not processed by the Radio Galaxy Zoo, which have a 'S_Code'='M', the RPA was determined by moment analysis. For the radio sources associated in the Radio Galaxy Zoo (hereafter LGZ sources), the RPA was the PA of the largest diameter vector of the source. The three ways would have consistent and reliable results for large, simple-structure sources. However, the measured RPA appeared to be biased significantly for small sources. In Fig. 5.1, we show the deconvolved RPA distribution of all the radio sources with a valid deconvolved RPA measurement ('DC_PA'> 0 in the LoTSS DR2 VAC) and a small RPA error ('E_DC_PA'$< 10^\circ$ in the LoTSS DR2 VAC). While the RPA of sources in the sky is expected to be uniformly distributed within 0° to 180°, the RPA distribution of the radio sources in the LoTSS DR2 has a prominent peak around 90°. We note that this bias is likely related to the actual beam shape in the LoTSS DR2. Given the complexity and uncertainty in the LOFAR radio image processing, we did not investigate further as it was not our focus in this work. We noticed that this bias is significant only for small sources. Therefore, we only included large sources that are not affected by the bias in this work.

To investigate which sources are large enough to be free from the 90° bias, we calculated the number of sources with RPA$= 60 - 120^\circ$, $n_{\rm peak}(A > A_{\rm min})$, and outside 60–120°, $n_{\rm outside}(A > A_{\rm min})$, for radio sources with an angular size A larger than $A_{\rm min}$. We defined the 'peak excess' as

$$X(A > A_{\rm min}) = 2n_{\rm peak}(A > A_{\rm min})/n_{\rm outside}(A > A_{\rm min}) \qquad (5.1)$$

and show the peak excess as a function of the minimum source size $A_{\rm min}$ ('Maj' or deconvolved size 'DC_Maj' in the LoTSS DR2 VAC) in Fig. 5.2. The peak excesses for all radio sources, single Gaussian radio sources and multiple Gaussian radio sources are listed from left to right respectively in Fig. 5.2.

Apparently, the 90° bias is more significant for small and single Gaussian sources. The source density at the peak RPA can be $\sim$1.5 to 2.6 times larger than the non-peak RPA regions for radio sources with an $A_{\rm min}$ of less than $8''$. For single Gaussian sources, the peak excess drops to 1.2 only for sources with an angular size larger than $\sim 25''$. The peak excess is less influential for multiple Gaussian sources as it drops to less than 1.1 at a minimum deconvolved angular size of $\sim 5''$.

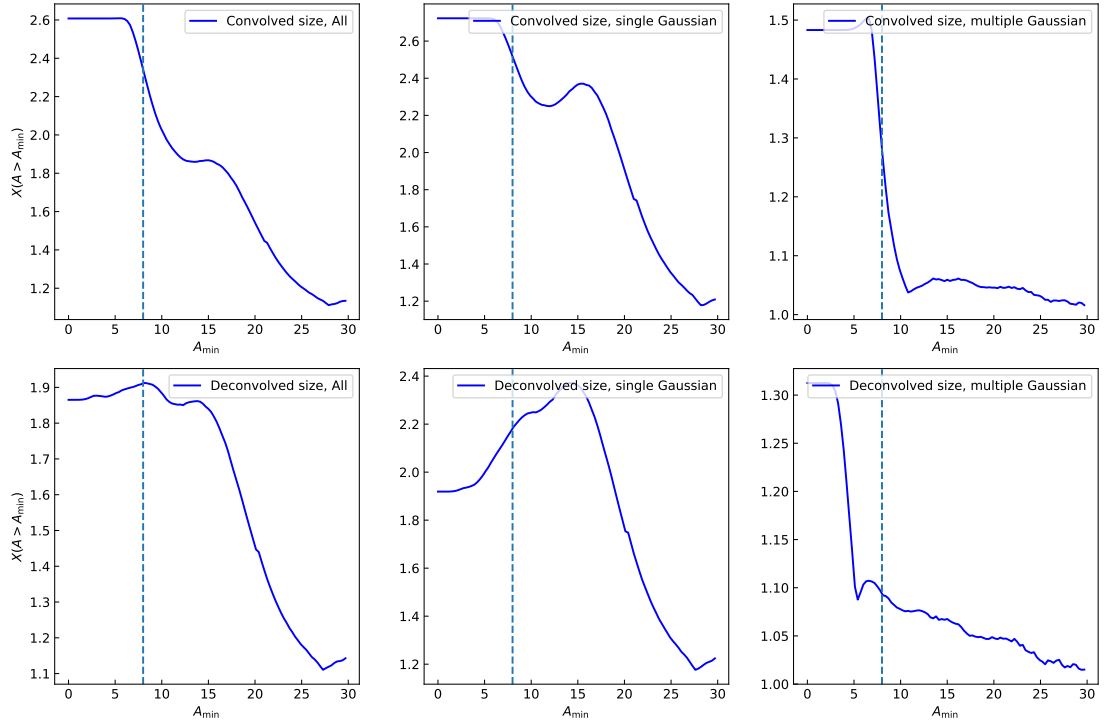

Figure 5.2: The peak excess $X(A > A_{\rm min})$ of radio sources in the LoTSS DR2 VAC with different minimum source angular sizes $A_{\rm min}$(convolved or deconvolved major axis). Top panels: the peak excess as a function of the minimum convolved sizes. Bottom panels: the peak excess as a function of the minimum deconvolved sizes. The peak excess for all radio sources, single Gaussian radio sources and multiple Gaussian radio sources are listed from left to right respectively. The dashed lines in each panel denote a minimum size of 8″.

Based on the peak excess results, we only select sources with a deconvolved angular size larger than 8″ to have an unbiased RPA measurement. The RPA distributions of these sources are shown in the right panel of Fig. 5.1. The 90° bias is not significant in these sources, but the distribution of RPA still differs from a uniform distribution. This deviation from uniformity might be related to the residual effect of the beam shape bias or an alignment of jets of unknown origin(e.g. Contigiani et al. 2017; Osinga et al. 2020). We note that this deviation is less than 10% different from the average value and will likely not influence our analyses significantly.

In addition, we also require the radio sources to be a resolved source in the LoTSS DR2 VAC.In LoTSS DR2, a source is marked as 'unresolved' when the ratio of integrated flux density (S_I) to the peak brightness (S_p) S_I/S_p is smaller than 99.9% of the isolated small single component sources ('S-sources' hereafter) with similar S/N across the entire field of view (FoV; Shimwell et al. 2022). This means that a source is more likely to be a point source rather than a source with extended structures (Shimwell et al. 2022). In this case, the shape of the radio source would be close to the beam shape and the RPA measured by moment analysis would not indicate the RPA of the physical radio source.

We also only selected simple radio sources with well-defined RPAs. We defined 'simple source' to be a source for which all the components are basically aligned in one direction, e.g. simple two-sided lobes. These sources have a well-defined RPA in contrast to those with X-shape or Z-shape structures or complex, blurred features. To select the simple radio sources, we calculated the component-determined RPA ($\mathrm{RPA_{comp}}$) for each LR-detected source, which is the PA of the vector linking the two brightest components of the source. For a simple radio source, the $\mathrm{RPA_{comp}}$ should be in line with the catalogue RPA, which was estimated by moment analyses taking all the components into account. The differences between the $\mathrm{RPA_{comp}}$ and the catalogue RPA, ΔRPA, are less than 20° for about 80% of the LR-detected sources. The rest of the LR-detected sources along with the LGZ sources, whose RPAs are based on visual checks, are assumed to be the sources with a well-defined RPA in this work.

In summary, we adopted the following criteria to select radio sources with an unbiased and well-defined RPA:

(1) the LR-detected sources with the measuring uncertainty of deconvolved RPA 'E_DC_PA'<10° , or the LGZ sources that are not likely to be blended or problematic sources ('Blend_prob' or 'Other_prob'

< 0.2 in the LoTSS DR2 VAC);[2]

(2) the deconvolved angular size 'DC_Maj'$> 8''$ or 'LGZ_Size' (size determined by the Radio Galaxy Zoo) $> 8''$;

(3) multiple Gaussian components sources ('S_Code'='M') or LGZ sources ('S_Code'='Z');

(4) keyword 'Resolved'='True' in the LoTSS DR2 VAC;

(5) ΔRPA<20° for LR-detected sources.

Optical positional angles

To obtain reliable jet-galaxy alignment measurements, it is also important to have reliable OPA measurements. Unfortunately, the errors of OPA in the Legacy Surveys were not provided. Considering that many sources in the Legacy Surveys also have detection in the SDSS and the PSF sizes in the two surveys are comparable (Dey et al. 2019), we assessed the reliability of OPAs in the Legacy Surveys by comparing the OPA measurements in the two surveys. Because the OPAs in the two surveys were measured independently, sources with OPA that can be measured reliably should have consistent OPAs in the two surveys. We show the OPAs of sources with a counterpart in both the Legacy Surveys and the SDSS ('LS-SDSS sources' hereafter) in our sample in Fig. 5.3. While most of these sources have consistent OPAs in the two optical surveys, a large number of sources have a poor-defined $\mathrm{OPA_{LS}}$ (0° in the Legacy Surveys) or inconsistent OPAs.

For each LS-SDSS source, we obtained the difference of OPAs in these two Surveys, $\Delta\mathrm{OPA}=|\mathrm{OPA_{LS}} - \mathrm{OPA_{SDSS}}|$. We investigated the change of the ΔOPA as a function of different morphological parameters in the Legacy Surveys and calculated the fraction of 'bad sources' ($\Delta\mathrm{OPA} > 20^\circ$). We found that the bad sources were primary sources with a size close to the PSF size or with a round shape (large axis ratio). Therefore, to obtain a sample with reliable OPA measurements, we include three more criteria in the sample selection process:

[2]The LGZ sources do not have an error estimation for RPA, but they are typically large and verified by human eyes. Therefore we assume they have negligible measurement errors. Instead, the possibility that they are blended sources or sources with other problems is used to evaluate the reliability of the measurement.

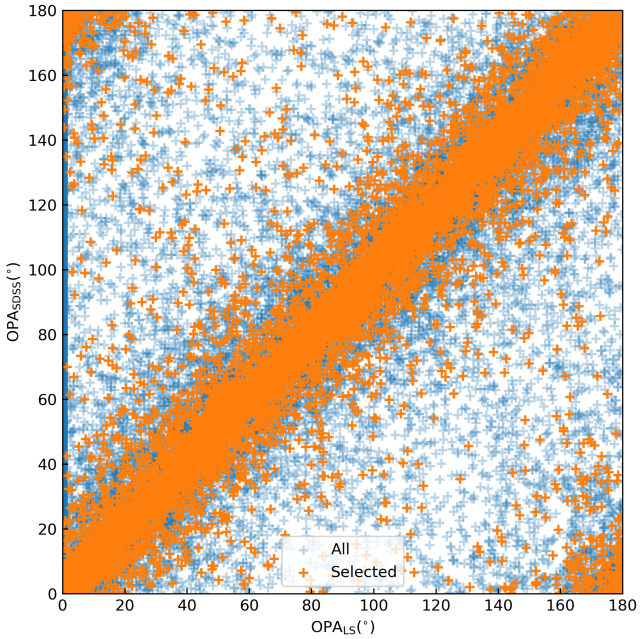

Figure 5.3: The OPAs of sources with detection in both the Legacy Surveys and the SDSS in this work. The x-coordinates denote the OPAs in the Legacy Surveys and the y-coordinates denote the OPAs in the SDSS. The blue points are all the LS-SDSS sources before adopting criteria (6)-(8). The orange points are the LS-SDSS sources selected by criteria (6)-(8).

(6) half-light radius in the Legacy Surveys $R_{50} > 1.5''$;

(7) $R_{50}/\mathrm{FWHM_{PSF}} > 1.2$, where $\mathrm{FWHM_{PSF}}$ is the FWHM of the PSF in the Legacy Surveys;

(8) optical axis ratio 'BA<0.8'.

After adopting these criteria, we show the OPAs of the remaining LS-SDSS sources in Fig. 5.3. We found that the sources with poor-defined $\mathrm{OPA_{LS}}$ or inconsistent OPAs were mostly removed. The fraction of bad sources in the remaining LS-SDSS sample was $\lesssim 10\%$.

By adopting these criteria (1)-(8), we selected 11 071 radio sources with reliable RPA and OPA in the LoTSS DR2 VAC. For simplicity, we called this sample the 'RO' sample hereafter.

Radio AGN classification

The radio emission from galaxies can be due to AGN activities or star formation (e.g. Condon 1992; Best et al. 2005b; Sabater et al. 2019). The radio emission from the AGNs usually takes the form of collimated jets, of which the direction should be related to the spin of the SMBH. In contrast, the emission from star formation would be spreading across a galaxy. Therefore, the radio emission of the star-forming (SF) galaxies is expected to be aligned with the optical major axis of the galaxy. This would become contamination in the jet-galaxy alignment analyses. To reduce the contamination from the SF galaxies, we need to identify the radio AGNs in the RO sample.

For most sources in the LoTSS DR2, spectroscopic information is not available, to separate the radio AGNs and star-forming galaxies, we used the WISE colours. As the W2 band captures the stellar emission and the W3 band the Polycyclic Aromatic Hydrocarbon (PAH) strength (Jarrett et al. 2011), which is an indicator for warm dust associated with SF, the W2-W3 colour is used to distinguish between star-forming and passive galaxies(Yan et al. 2013; Cluver et al. 2014; Herpich et al. 2016). Because the host galaxies of radio AGNs and SF galaxies tend to have different star formation rate(SFR; e.g. Heckman & Best 2014), the W2-W3 colour has also been used to select radio AGN in Sabater et al. (2019) and Hardcastle et al. (2019). Only using the W2-W3 colour might only recover part of the radio AGNs population as it does not take the radio information into account explicitly. We therefore introduce the radio luminosity-WISE colour diagram to the radio AGN selection process.

We show the logarithmic radio luminosity at 150 MHz $\log(L_{150\,\mathrm{MHz}}/(\mathrm{W\,Hz^{-1}}))$ as a function of the W2-W3 AB colour for the low redshift sources ($z < 0.5$) in the RO sample in the left panel of Fig.5.4. Apparently, the sources can be divided into two populations, which cluster in two regions in the radio luminosity-WISE colour diagram. As suggested by Gürkan et al. (2018), the radio emission from star-formation could hardly reach $L_{150\,\mathrm{MHz}} > 10^{25}\,\mathrm{W\,Hz^{-1}}$, the population on the top left region in the radio luminosity-WISE colour diagram (high radio luminosity, small W2-W3) should be associated with radio AGNs. The fainter and bluer population should be SF galaxies.

For comparison, we also plot the radio sources in Sabater et al. (2019) with detailed AGN/SF classifications based on LoTSS DR1 data in the right panel of Fig.5.4. While the radio sources in the Sabater et al. (2019) in

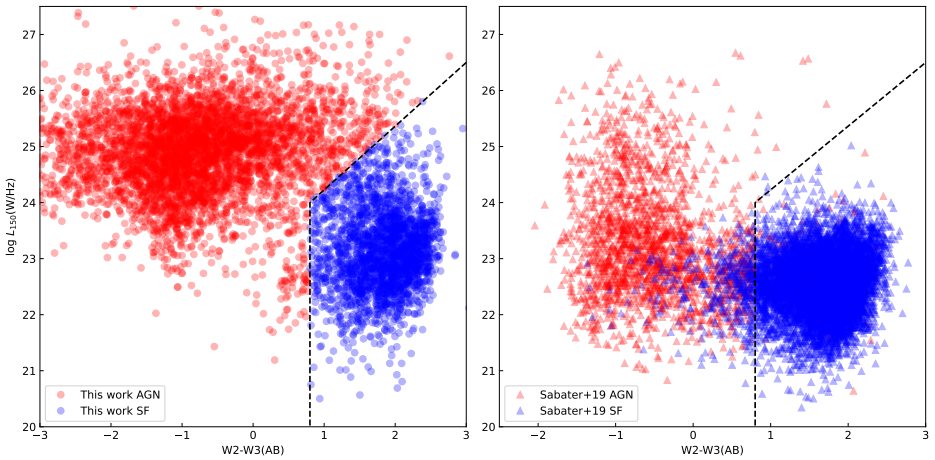

Figure 5.4: Radio luminosity-WISE colour diagram for low redshift radio sources in LoTSS. Left: the radio luminosity and W2-W3 AB colours for the radio sources with $z < 0.5$ in the RO sample in this work. The red and blue circles show the radio AGN and SF galaxies classified in this work respectively. Right: the radio luminosity and W2-W3 AB colours for the sources in Sabater et al. (2019) based on the low redshift LoTSS DR1 sample ($z < 0.3$). The red and blue triangles denote the radio AGN and SF galaxies classified based on radio luminosity, spectroscopic information and WISE colours in Sabater et al. (2019). The dashed lines in the two panels show the AGN/SF division lines used in this work.

general have lower radio luminosity, they also show a similar bimodality in the radio luminosity-WISE colour diagram with most of their SF galaxies in the bluer region and the radio AGNs in the red region. This is not surprising because Sabater et al. (2019) used the W2-W3 colour as an auxiliary method in their AGN/SF classification. They used a simple division of W2-W3=0.8 and found the WISE-colour classifications were highly consistent with the classifications based on the radio luminosities and spectroscopic information. But this simple division would fail to separate the two populations for high luminosity sources in the RO sample.

To make our classification consistent with previous results, we classified low luminosity sources ($L_{150\,\mathrm{MHz}} < 10^{24}\,\mathrm{W\,Hz^{-1}}$) with W2-W3<0.8 to be radio AGNs, while at high luminosities we chose radio AGNs to be the sources with $\log(L_{150\,\mathrm{MHz}}/(\mathrm{W\,Hz^{-1}})) > 24 + (\mathrm{W2} - \mathrm{W3} - 0.8) \times 2.08$, which was based on human-eye inspection on the low redshift RO sample. We applied our division lines for the sample in Sabater et al. (2019) in the right

panel of Fig. 5.4 and they were consistent with the AGN/SF classifications at high luminosities. Our AGN/SF classifications successfully reproduced ∼95% of the classification results in Sabater et al. (2019), which were based on more sophisticated methods.

Based on the radio luminosity-WISE colour diagram, we classified 3294 low redshift radio AGNs and 3368 low redshift SF galaxies. We call them 'LowzROAGN' and 'LowzROSF' in the following analyses. While our W2-W3 division lines showed a classification accuracy of about 95% for the low luminosity sample in Sabater et al. (2019), we suggest that our classifications would have a higher accuracy in our sample, which have a larger fraction of radio sources with $L_{150\,\mathrm{MHz}} > 10^{24}\,\mathrm{W\,Hz^{-1}}$.

FIRST sample

To compare with previous work (Battye & Browne 2009), we also used data from the FIRST survey. The FIRST survey covers 10,000 square degrees of the north and south galactic caps (Becker et al. 1995) and produces roughly 946,000 sources at a resolution of $5''$, and a typical rms of $0.15\,\mathrm{mJy}$ over 92 square degrees. A median rms noise of $52\,\mu\mathrm{Jy\,beam^{-1}}$ was achieved. At the detection threshold of $1\,\mathrm{mJy}$, the number of sources per square degree is roughly 90, and approximately 35% of the sources have resolved structure on 2-30″ scales with 30% of sources having counterparts in SDSS (Domínguez Sánchez et al. 2022).

We used the radio sample described in Best & Heckman (2012), which contains 18 286 radio sources with an optical counterpart in the SDSS data release 7 (Abazajian et al. 2009). These sources were further cross-matched with the photometric and spectroscopic data using `CasJobs`[3] based on their object IDs. For the sources, we obtained the OPAs and host galaxy properties including stellar mass ($M_\star$), SFR, axis ratio (b/a; a and b are apparent major and minor axes of the host galaxy), the flux of the doubly ionized oxygen ([O[III]) emission line, and the velocity dispersion (σ). The host galaxy properties were based on the Max Planck for Astrophysics and Johns Hopkins University groups' (MPA-JHU) spectroscopic reanalysis within the SDSS database (Brinchmann et al. 2004). In this way, we obtain 17,165 sources. We also applied restrictions mentioned in Battye & Browne (2009). All galaxies classified as 'stellar' through the SDSS pipeline were excluded first, followed by the elimination of faint sources

[3] `https://skyserver.sdss.org/CasJobs/`

Sample	Number of sources
LowzROAGN	3 294
FIRSTAGN	2 336
LowzROSF	3 368
FinAGN	5 350

Table 5.1: The number of sources in the low redshift radio samples selected in this work.

with $r > 18$ where r is the r band magnitude, $b/a > 0.8$, and sources with a deconvolved angular size less than 2″. In addition, we only took radio AGNs classified in Best & Heckman (2012) using methods similar to the Sabater et al. (2019). After the restrictions, we obtained a sample called 'FIRSTAGN' containing 2 336 AGN with redshift $z < 0.5$. We note that the selection criteria for the sources in FIRST are not the same as those for the LoTSS sources. However, we checked that the RPA distribution of the selected sources does not show significant bias and Battye & Browne (2009) also suggested that the OPA are reliable. Furthermore, we found 280 AGNs appearing in both the FIRSTAGN and the LowzROAGN samples. These overlapping sources have independent but consistent RPA and OPA measurements in the two samples. We therefore suggested that the RPAs and OPAs in the FIRSTAGN sample are reliable and consistent with those in the LowzROAGN sample.

5.2.3 Summary of the samples

In summary, we selected two low redshift radio AGN samples and an SF galaxy sample based on the LoTSS DR2 and the FIRST data. We list the number of sources of these samples in Tab. 5.1. For the following analyses, we merged the FIRSTAGN and LowzROAGN samples into a final radio AGN sample 'FinAGN' containing 5350 sources. For the sources appearing in both samples, their RPA and OPA are taken as the average of the measurements in the two radio and optical surveys.

For the radio samples based on the LoTSS DR2, we estimated their stellar masses using the $M_\star - \nu L_\nu(3.4\,\mu\mathrm{m})$ relations (Wen et al. 2013) for AGNs,

$$\log(\frac{M_\star}{M_\odot}) = 1.132 + \log(\frac{\nu L_\nu(3.4\,\mu\mathrm{m})}{L_\odot}) \tag{5.2}$$

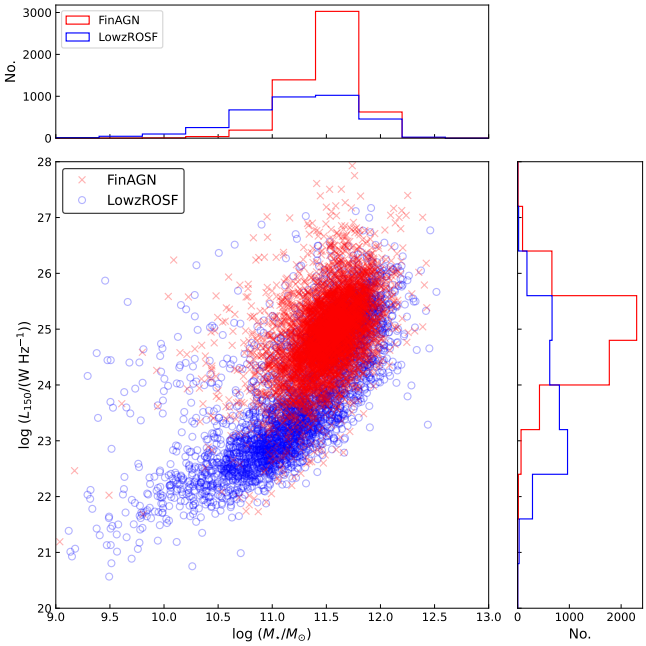

Figure 5.5: The $M_\star$ and $L_{150\,\mathrm{MHz}}$ distributions of the radio samples selected in this work. In the major panel, sources in the FinAGN and LowzROSF samples are denoted by red crosses and blue empty circles respectively. Top: the $M_\star$ distributions of the four samples. The FinAGN and LowzROSF samples are shown in red and blue histograms respectively. Right: the $L_{150\,\mathrm{MHz}}$ distributions of the two samples.

and for SF galaxies,

$$\log(\frac{M_\star}{M_\odot}) = -0.04 + 1.12\log(\frac{\nu L_\nu(3.4\,\mu\mathrm{m})}{L_\odot}) \tag{5.3}$$

where $\nu L_\nu(3.4\,\mu\mathrm{m})$ is the rest frame 3.4 μm radio luminosity. The derived $M_\star$ are consistent with the results based on spectroscopic analysis for the sources with SDSS data with a difference of $\lesssim$0.2 dex. This was also confirmed in Wen et al. (2013).

We show the $M_\star$ and $L_{150\,\mathrm{MHz}}$ distributions of the FinAGN and LowzROSF samples in Fig. 5.5. For sources from the FIRSTAGN sample, the $L_{150\,\mathrm{MHz}}$ are estimated assuming a canonical radio spectral index of 0.7 (Condon et al. 2002). From Fig. 5.5, we can see that our radio AGN samples are typically with $M_\star$ ranging from 10^11 to $10^{12}\,M_\odot$ and $L_{150\,\mathrm{MHz}}$ ranging from 10^{23} to

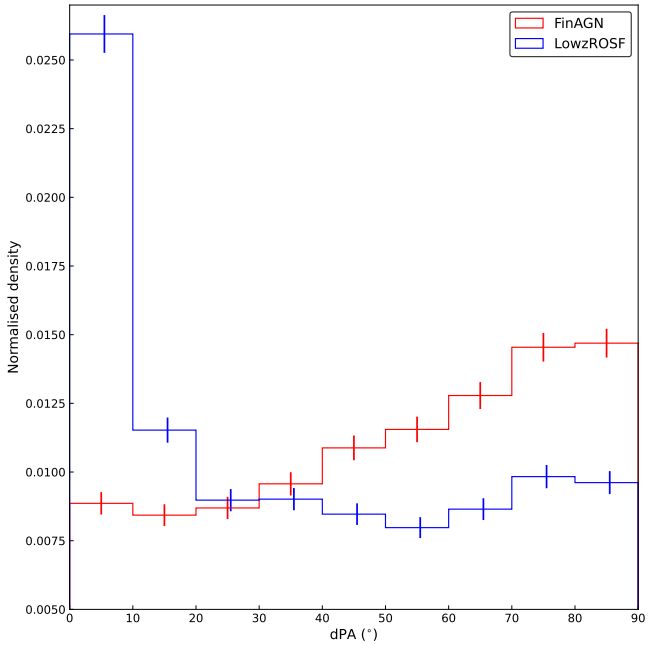

Figure 5.6: The alignment distributions for the two samples. The marker of different samples is in the same manner as in the top panel of Fig.5.5. The errorbars for the LowzROSF sample are offset for clarity.

10^{27} W Hz^{-1}. In contrast, the SF galaxies have a higher fraction of low $M_\star$ and low $L_{150\,\mathrm{MHz}}$ sources.

5.3 Radio-optical alignment distribution

To investigate the orientation of the radio jets with respect to their host galaxies, we defined the radio-optical alignment of a galaxy, noted as dPA, to be the apparent difference between the galaxy's RPA and OPA. In Fig. 5.6, we show the alignment distributions for the FinAGN and LowzROSF samples.

Apparently, the dPA of radio AGNs and SF galaxies are significantly different. The distributions of dPA for the radio AGNs are biased towards 90° . This prominent minor-axis alignment tendency indicates that for the majority of radio AGNs, the apparent jet orientations are nearly perpen-

dicular to their galactic plane. In contrast, the dPAs of the SF galaxies are significantly biased towards 0°, indicating that the radio emission of the galaxies is aligned with the optical images. This major-axis alignment tendency agrees with the idea that the radio emission from the SF galaxies originates from the star formation activity across the galactic plane. The difference in the alignment distributions for radio AGNs and SF galaxies confirmed the reliability of our radio AGN/SF classification using the WISE colours.

5.3.1 $L_{150\,\mathrm{MHz}}$ and $M_\star$ divisions

Radio AGNs with different luminosities and $M_\star$ exhibit different physical properties (see e.g. Janssen et al. 2012; Heckman & Best 2014; Zheng et al. 2020), which implies different physical processes in these AGNs. In this section, we further investigate the dPA for sources with different $M_\star$ and radio luminosity, by dividing the samples into different groups for alignment analysis based on their radio luminosity $L_{150\,\mathrm{MHz}}$ and the $M_\star$ of their host galaxy.

Based on the $L_{150\,\mathrm{MHz}}$ distributions, to ensure comparable numbers of sources in different groups, we divided the entire sample into bright and faint sources depending on whether they have $L_{150\,\mathrm{MHz}}$ larger or lower than $10^{25}\,\mathrm{W\,Hz^{-1}}$. The two groups contain 2427 and 2923 sources respectively. The corresponding dPA tendencies are shown in the upper panels of Fig. 5.7. The radio AGNs are basically minor-axis aligned regardless of their luminosities. We performed a Kolmogorov-Smirnov (K-S) test on the two dPA distributions and the result showed a null hypothesis probability (p_{null}) of 12.9%. This indicates that the two dPA distributions do not show a significant difference.

Intriguingly, we found the dPA distributions for the fainter group seem to have a minor up-turn at dPA$< 15^\circ$. This could be the contamination from SF galaxies or a real secondary population as mentioned in Battye & Browne (2009).

The sample was also separated into massive and less massive groups based on whether their $M_\star$ are larger than $10^{11.5}\,M_\odot$. The two groups contain 2893 and 2457 sources respectively. The dPA distributions of massive and less massive galaxies are shown in the lower panels of Fig. 5.7. Similar to the $L_{150\,\mathrm{MHz}}$ -divided results, the dPA distributions show similar minor-axis alignment tendencies in both two groups. But the less massive galaxies have a lower peak while the massive galaxies also show a minor

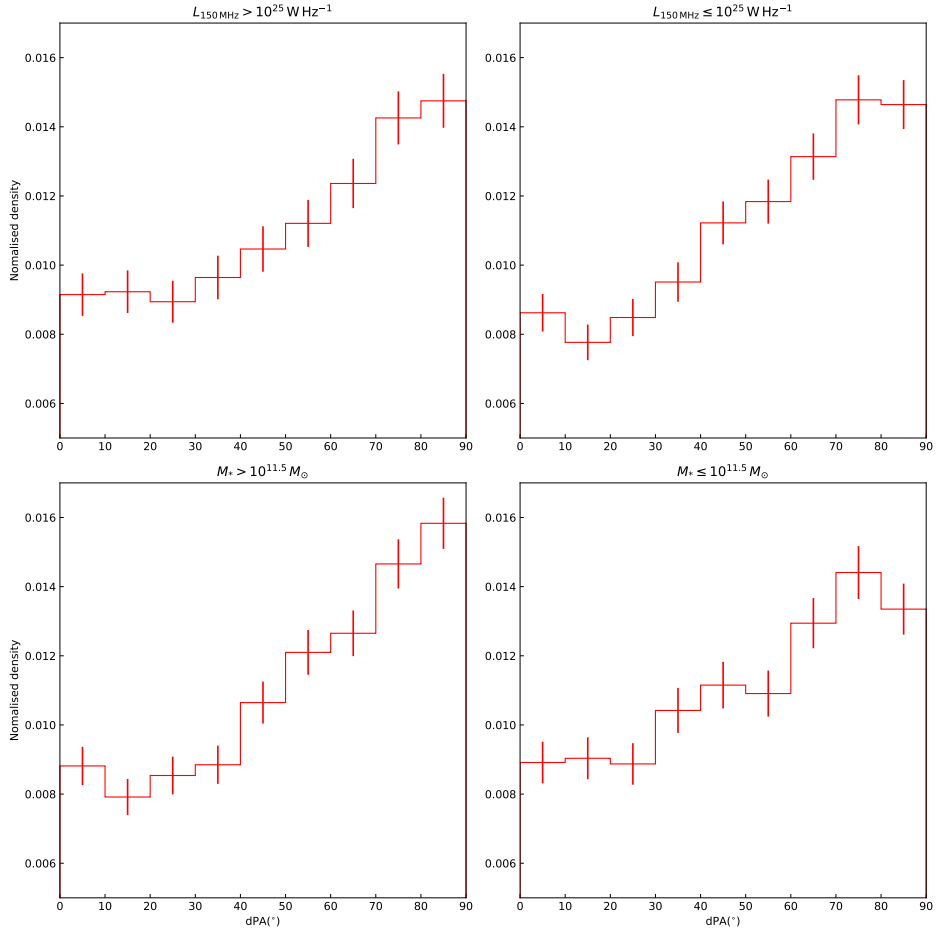

Figure 5.7: The dPA distributions for radio AGNs with different $L_{150\,\mathrm{MHz}}$ and $M_\star$. Top (left to right): The alignment distributions of bright ($L_{150\,\mathrm{MHz}} > 10^{25}\,\mathrm{W\,Hz^{-1}}$) and faint ($L_{150\,\mathrm{MHz}} \leqslant 10^{25}\,\mathrm{W\,Hz^{-1}}$) radio AGNs. Bottom (left to right): The alignment distributions of massive ($M_\star > 10^{11.5}\,M_\odot$) and less massive ($M_\star \leqslant 10^{11.5}\,M_\odot$) radio AGNs.

up-turn below 15° . The K-S test result indicates a p_{null}=1.4%, which tends to reject the null hypothesis that the two dPA distributions are similar.

The upturn tendency at small dPAs in the alignment distribution is likely to be related to both $L_{150\,\mathrm{MHz}}$ and $M_\star$, hence purely $L_{150\,\mathrm{MHz}}$ or $M_\star$-divided analyses might weaken the trend. To further investigate this weak

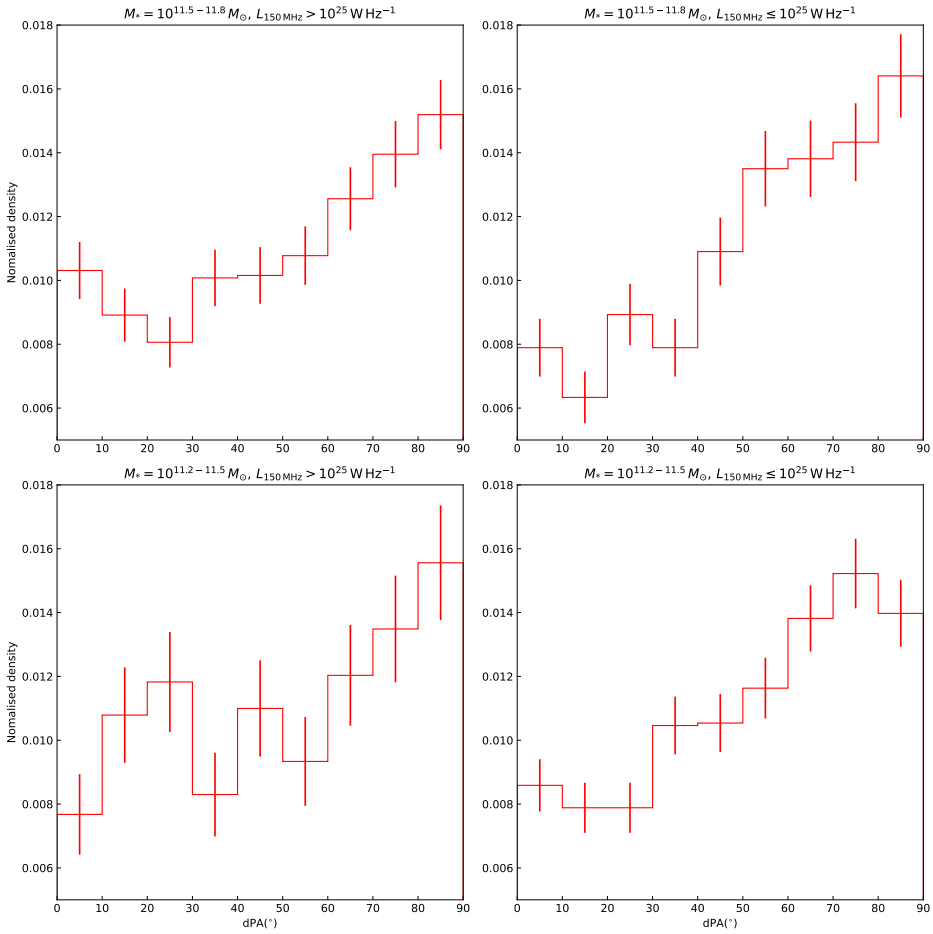

Figure 5.8: Alignment distributions of radio AGN with different radio luminosities in two $M_\star$ bins. Top (left to right): The alignment distributions of bright ($L_{150\,\mathrm{MHz}} > 10^{25}\,\mathrm{W\,Hz^{-1}}$) and faint($L_{150\,\mathrm{MHz}} \leqslant 10^{25}\,\mathrm{W\,Hz^{-1}}$) radio AGNs with $M_\star$ ranging from $10^{11.5}$ to $10^{11.8}$ $M_\odot$. Bottom (left to right): The alignment distributions of bright and faint radio AGNs with $M_\star$ ranging from $10^{11.2}$ to $10^{11.3}$ $M_\odot$.

major-axis alignment tendency, we check the alignment distributions in two narrow $M_\star$ bins with large numbers of sources. The first category includes AGNs with $M_\star$ between $10^{11.5}$ and $10^{11.8}$ $M_\odot$, while the second category includes AGNs with $M_\star$ between $10^{11.2}$ and $10^{11.5}$ $M_\odot$. These two categories of AGNs were then further divided according to whether they

are brighter or fainter than $L_{150\,\mathrm{MHz}} = 10^{25}\,\mathrm{W\,Hz^{-1}}$.

Fig. 5.8 shows the dPA distributions of radio AGNs with different $L_{150\,\mathrm{MHz}}$ in the two $M_\star$ bins. The numbers of sources in the four groups are 1290, 963, 482 and 1281 respectively (from top left to bottom right in Fig. 5.8). Generally, the dPA distributions in the four groups all show a minor-axis alignment. We performed K-S tests to compare the dPA distributions in every two groups. The K-S test results only indicate a p_{null} smaller than 5% in tests for the bright&massive and the faint&massive groups (the two top panels in Fig. 5.8) and for the faint&massive and the bright&less massive groups (the top right and the bottom left panels). We note that except for the faint&massive group, all other three groups seem to show a flatten or up-turn trend at small dPAs.

The stronger major-axis alignment tendency in the two bright samples implies that the major-axis alignment tendency is not likely to be the contamination of SF galaxies, because the SF contamination should be largest for less massive and low-luminosity populations (Best & Heckman 2012; Sabater et al. 2019). We suggest that the difference in the apparent dPA distribution reflects the difference in the intrinsic jet-galaxy alignment between the bright sources and the faint ones.

5.3.2 Galaxy morphology dependence

Recent studies suggested that powerful radio jets tend to reside in round galaxies (e.g. Barišić et al. 2019; Zheng et al. 2020). This trend might be the result of the central black holes of galaxies with a merger-dominant assembly history having a different distribution of spin compared to galaxies with a more quiescent history (Zheng et al. 2023). If this hypothesis is correct, then we should be able to see different dPA distributions for round and elongated galaxies.

We chose the axis ratio $b/a = 0.7$ to divide the samples into two groups with comparable numbers of sources. The dPA distributions of the radio AGNs with different $L_{150\,\mathrm{MHz}}$ in the two groups are shown in Fig. 5.9. The four groups contain 1232, 1622, 1195 and 1301 sources respectively. Most of the dPA distributions still show an overall minor-axis alignment tendency in all four groups. However, the minor axis alignment tendency seems to be much weaker in the two round groups. While for the elongated groups, the numbers of sources with dPA$\simeq$90° are about two times the numbers at $\leqslant$ 30° , the highest source numbers in the round groups are only $\sim 40\%$ larger than the lowest point. This could be a projection effect if the intrinsic jet is

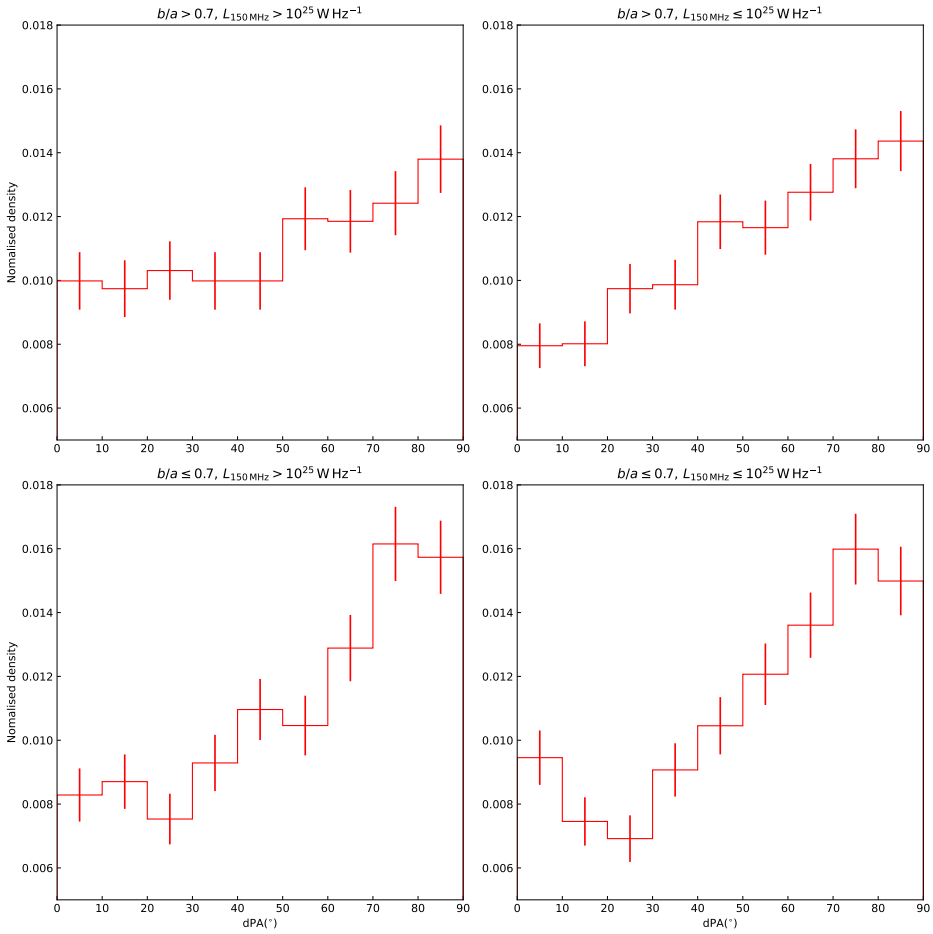

Figure 5.9: Alignment distributions of radio AGN with different radio luminosities in two morphology groups. Top (left to right): The alignment distributions of bright radio AGNs with $b/a > 0.7$. Bottom (left to right): The alignment distributions of bright and faint radio AGNs with $b/a \leqslant 0.7$.

aligned roughly with the minor axis of the host galaxy. In this scenario, as the apparent round galaxies are more likely to be face-on, the apparent dPA would become largely affected by the intrinsic offset between the jet and the minor axis of the galaxy and the measurement uncertainties, which tend to flatten the dPA distribution. This projection effect will be discussed further in Sect. 5.4.

We performed K-S tests on each pair of groups with similar axis ratio ranges (i.e. in the same row in Fig. 5.9). For the round groups, the test rejected the null hypothesis with a $p_{\rm null} = 4.7\%$, indicating a significant difference between the bright and faint samples. Therefore, for the round radio galaxies, the apparent jet alignment is dependent on the radio luminosity with the fainter radio jets being more aligned with the minor axis of the host galaxies. In contrast, the $p_{\rm null}$ is 79.6% for the elongated groups and the null hypothesis could not be rejected. Perhaps the reason for this is that the prevalence of a strong minor-axis alignment tendency in the two groups makes it more difficult to discern a subtle difference.

5.4 Apparent alignment to intrinsic alignment

The presented analyses are based on the projected alignment measured directly from radio and optical images. In this section, we investigate the intrinsic AGN jet orientations based on some simple assumptions.

5.4.1 Finding the Oblate Galaxy Fraction

To produce a simulation of the projection effect, we need to model the real spatial orientations of radio AGN jets in relation to their host galaxies. We first estimate the galaxy shape distributions statistically in a simpler way. We assume that the entire galaxy population can be divided into two different groups based on their shapes, i.e. oblate galaxies and triaxial galaxies (Chang et al. 2013). Oblate galaxies have two equal-sized axes and a shorter z-axis, corresponding to galaxies with a prominent disc component. Triaxial galaxies have three axes with different sizes, corresponding to elliptical galaxies. A sample with only triaxial galaxies or oblate galaxies results in different apparent axis ratio distributions. The axis ratio distribution of a galaxy sample can be decomposed into an oblate and a triaxial component, thus providing information about the distribution of the intrinsic shape of the galaxies in the sample. The fraction of oblate galaxies and triaxial galaxies can then be used to reproduce the apparent alignment distribution.

To simulate the axis ratio of triaxial and oblate galaxies, we follow the recipes in Chang et al. (2013) to simulate the oblate and triaxial populations, assuming the three axes of a galaxy to be $a \geqslant b \geqslant c$. The oblate galaxies are taken to have a mean intrinsic axis ratio $\epsilon = b/a = c/a = 0.29$

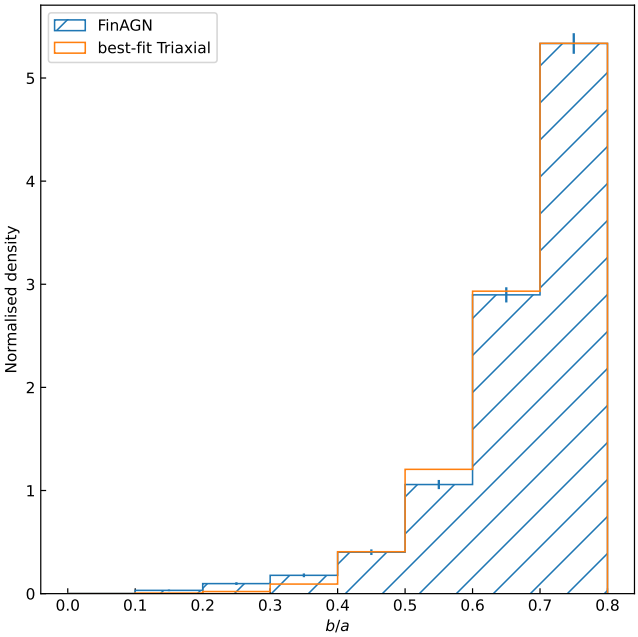

Figure 5.10: The normalised apparent axis ratio distributions for the FinAGN sample and the best-fit triaxial model. The blue hatch histogram denotes the FinAGN sample while the orange histogram denotes the triaxial model.

and a standard deviation of $\sigma_\epsilon = 0.07$. The triaxial galaxies are described by two parameters, $T(=[1-\beta^2]/[1-\gamma^2])$ and $E(=1-\gamma)$ where $\beta = b/a$ and $\gamma = c/a$. The T follows a Gaussian distribution with a mean of $T = 0.64$ and a standard deviation of $\sigma_T = 0.08$. The E has a mean value of $E = 0.41$ and a standard deviation of $\sigma_E = 0.19$.

We define the galaxy's frame (x, y, z) with the x-axis along the major axis of the galaxy and z-axis along the minor axis, and an observer's frame (x', y', z') with z'-axis pointing from the centre of the galaxy to the observer and x'-axis in the xy plane. For an observer at LOS with polar coordinates (θ, ϕ) in the galaxy's frame, Binney (1985) gave the equation for the projected ellipse as

$$R^2 = Ax'^2 + Bx'y' + Cy'^2 \tag{5.4}$$

where R is a radius-related constant and

$$A \equiv \frac{\cos^2\theta}{\beta^2}(\sin^2\phi + \frac{\cos^2\phi}{\gamma^2}) + \frac{\sin^2\theta}{\gamma^2}\,, \tag{5.5}$$

$$B \equiv \cos\theta \sin 2\phi (1 - \frac{1}{\gamma^2})\frac{1}{\beta^2}\,, \tag{5.6}$$

$$C \equiv (\frac{\sin^2\phi}{\gamma^2} + \cos^2\phi)\frac{1}{\beta^2}\,. \tag{5.7}$$

The projected apparent axis ratios q of the galaxy is then,

$$1 \geqslant q(\theta, \phi, \beta, \gamma) = \sqrt{\frac{A + C - \sqrt{(A-C)^2 + B^2}}{A + C + \sqrt{(A-C)^2 + B^2}}}\,, \tag{5.8}$$

To model the axis ratio distribution, we created a sample of 10 000 galaxies and simulated apparent axis ratio distributions for both the oblate and the triaxial populations. Defining the fraction of oblate galaxies in a sample to be $f_{\rm ob}$. We combined two axis ratio distributions with different $f_{\rm ob}$ and compared them with the observed axis ratio distributions. Additionally, the fit was performed only using the observed/simulated apparent axis ratio between 0 and 0.8 to match the source selection processes in Sect. 5.2.2.

We found the best-fit oblate fraction for the FinAGN sample with the minimum χ^2 statistics is 0, indicating a single triaxial component in the axis ratio distribution. This is in line with the implications in Barišić et al. (2019) and Zheng et al. (2020) that powerful radio AGNs are mostly triaxial galaxies.

As the fitting result indicated a pure triaxial population for the FinAGN sample, we varied the T, E, σ_T and σ_E with a step of 0.02 and generated triaxial models to fit the axis ratio distribution of the FinAGN sample. We found the best-fit T and E to be 0.84 and 0.2 respectively while the σ_T and σ_E were not changed. The modelled and observed axis ratio distributions are shown in Fig. 5.10.

5.4.2 Simulation of the dPA distribution

While measuring the intrinsic jet orientations in a large sample from imaging is difficult, we can study it statistically by reproducing the apparent alignment distributions with simple modelled intrinsic orientations. For

Figure 5.11: The distributions of the simulated jet pointing following Eq. 5.9 with different σ_j, 20° , 40° and 60° . The LOS in each plot is along the minor axis of the galaxy. The σ_j used in each panel is listed on top of the panel. Each plot contains 1 000 different jet pointing.

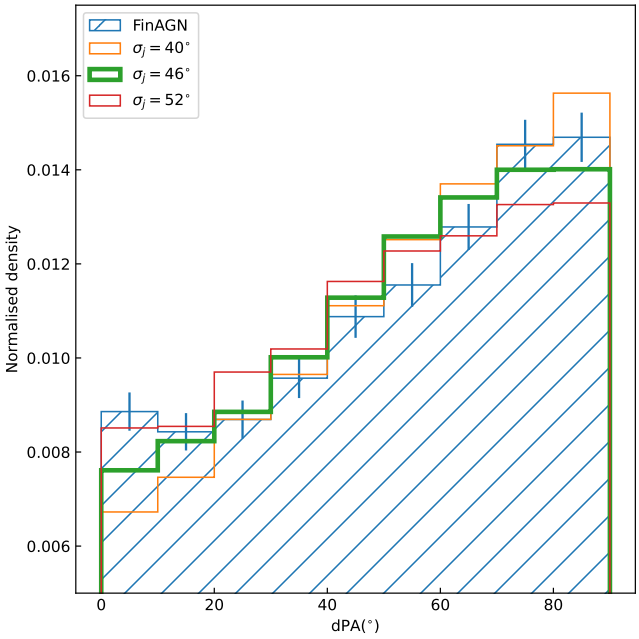

Figure 5.12: The simulated dPA distributions compared with the dPA distribution of the FinAGN sample. The hatched histogram with errorbars denotes the FinAGN sample. The σ_j for three simulated distributions are listed in the figure. The K-S tests indicate a largest $p_{\rm null}$ when $\sigma_j = 46^\circ$, which is marked with thick lines in the figure.

given LOS angles (θ, ϕ), we first calculated the PA of the apparent major axis of the projected galaxy, which has an intrinsic T, E as the best-fit model in the previous section. The PA of the apparent major axis can be derived from Eq. 5.4 as described in Binney (1985)[4]. For a jet pointing from the galactic centre to direction (θ_j, ϕ_j), where the polar coordinates are in the galaxy's frame, the apparent PA can be obtained by projection from the galaxy's frame to the $x'y'$ plane. In this way, we can obtain the apparent dPA for a jet observed from a given LOS.

We assumed the intrinsic offset between the jet and the minor axis of

[4]We note that the PA of the major axis calculated in this way does not follow a uniform distribution because the real north-south direction for an observer on earth is not taken into account in the calculation. This corresponds to a rotation along the z'-axis of the observer's frame (a different x'-axis). However, such rotation would be applied to both the apparent major axis and the apparent jet and the final dPA would not change.

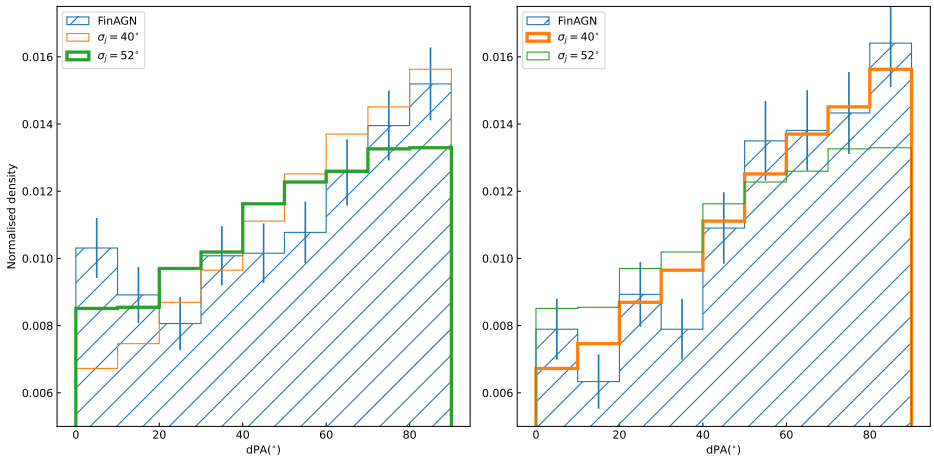

Figure 5.13: (From left to right) The simulated dPA distributions compared with the dPA distribution of the bright&massive and the faint&massive sample. The hatched histograms with errorbars denote the observed distributions in each panel. The σ_j for two simulated distributions are listed in the two panels. The simulated distribution corresponding to the largest $p_{\rm null}$ in each sample is highlighted in each panel.

the galaxy θ_j to follow a Gaussian distribution with a standard deviation of σ_j at a fixed ϕ_j. Then the overall probability density function of the θ_j is

$$p_{\rm gaus}(\theta_j|\sigma_j) \propto \sin(\theta_j)\frac{\exp(\frac{\theta_j^2}{2\sigma_j^2})}{\sigma_j}, \quad (0 \leqslant \theta_j \leqslant 90^\circ). \tag{5.9}$$

The σ_j can be used to estimate the level of the minor-axis alignment. As shown in Fig.5.11, a smaller σ_j suggests more jets are close to the minor axis.

For each σ_j from 30° to 60° with a step of 2°, we generated 100 000 galaxies with T and E following a best-fit distribution, 100 000 different jets angles following the distribution of Eq. 5.9, and 100 000 uniformly distributed LOS angles[5]. To match the data selection processes for the observed data, we excluded the simulated sources with an apparent axis ratio larger than 0.8. Finally, we obtained the simulated dPA distributions for each σ_j.

[5] $p(\theta) \propto \sin(\theta)$ and $p(\phi) = \text{Constant}$

5.4.3 Comparing Model to Observation

To find a jet distribution model that matches the FinAGN sample, we calculated the K-S statistics using the dPAs of the FinAGN sample and the modelled dPAs. The K-S results showed that the largest $p_{\rm null}$ is 8.8%, corresponding to a $\sigma_j = 46^\circ$. We showed the dPA distribution with $\sigma_j = 46^\circ$ along with the dPA distribution of the FinAGN sample in Fig. 5.12. To show the change of dPA distributions with σ_j, we also plotted two dPA distributions with $\sigma_j = 40^\circ$ and 52°, which have $p_{\rm null} \ll 1\%$. We also compared the simulated dPA distributions with the bright&massive and faint&massive samples in Sect. 5.3.1. The K-S tests indicate a largest $p_{\rm null} = 18.9\%$ at $\sigma_j = 52^\circ$ for the bright&massive sample and a largest $p_{\rm null} = 52.9\%$ at $\sigma_j = 40^\circ$ for the faint&massive sample. These results are shown in Fig. 5.13. We note that the models with $\sigma_j = 48 - 58^\circ$ all have a $p_{\rm null} > 5\%$ for the bright&massive sample. For the faint&massive sample, the models with $\sigma_j = 36 - 42^\circ$ all have a $p_{\rm null} > 5\%$. This result suggests that radio jets with higher luminosity in general have a larger offset with respect to the minor axis of the host galaxies.

We note that although the K-S results suggest no significant difference between the dPA distributions of the observed samples and some of the simulated dPA distributions, they do not indicate that these models fit well. As shown in Fig.5.12 and Fig.5.13, the simulated dPA distributions with the largest $p_{\rm null}$ can be outside the 1-σ limit in the histograms. We calculate the reduced χ^2 for these dPA distributions with 20° bins, and none of the results for the FinAGN and the bright&massive sample indicates a good fit (χ^2/d.o.f close to 1, where d.o.f is the degree of freedom in the fitting). This indicates that a single Gaussianised θ_j distribution is not adequate to describe the apparent dPA distributions.

To better mimic the intrinsic jet alignment, we use a two-component model to describe the θ_j distribution,

$$p(\theta_j|w) = w p_{\rm gaus}(\theta_j|20^\circ) + (1-w) p_{\rm gaus}(\theta_j|60^\circ) \tag{5.10}$$

The θ_j distributions for the two components $p_{\rm gaus}(\theta_j|20^\circ)$ and $p_{\rm gaus}(\theta_j|60^\circ)$ are shown in the first and the third panels of Fig. 5.11. The first component represents a population in which the jets are more likely to be aligned to the minor axis of the galaxy, while the second component represents a population with more randomly pointing jets. Note that the choice of 20° and 60° is based on the need to have a minor-axis aligned component and a less aligned component and the two components should be one larger

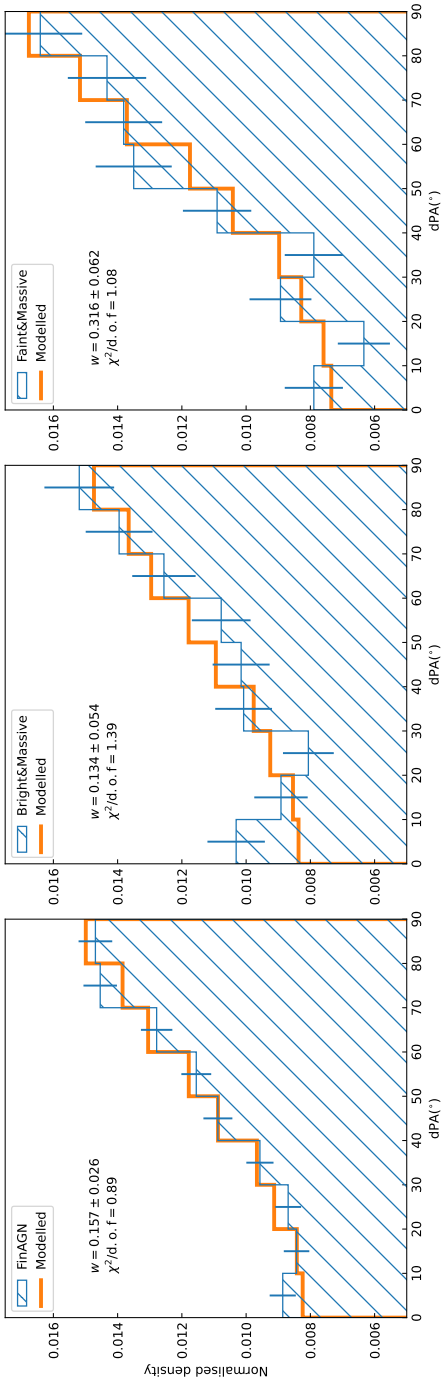

Figure 5.14: (From left to right) The two-component simulated dPA distributions compared with the dPA distribution of the FinAGN, the bright&massive and the faint&massive sample. The hatched histograms with errorbars denote the observed distributions in each panel. The best-fit simulated distributions are highlighted with thick lines in all panels.

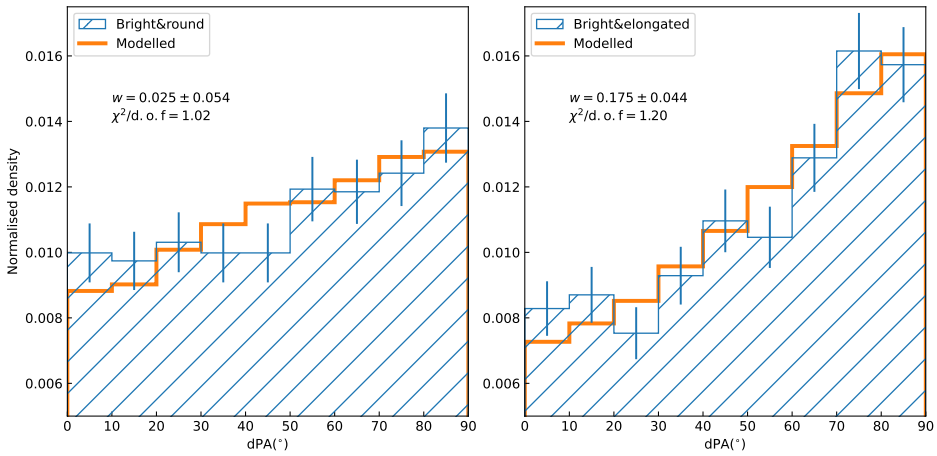

Figure 5.15: (From left to right) The two-component simulated dPA distributions compared with the dPA distribution of the bright&round and the bright&elongated sample defined in Sect. 5.3.2 . The hatched histograms with errorbars denote the observed distributions in each panel. The best-fit simulated distributions are highlighted with thick lines in all panels.

than the best-fit angle in the single component fitting ($\sim 46°$) and the other smaller than that. Other combinations of angles might also work as long as they can provide good fits as the model in this work.

We used the least-square method to find the best-fit weights w of the first component for the FinAGN sample, the bright&massive and the faint&massive samples. The best-fit results are shown in Fig. 5.14 and Tab. 5.2. We can see that the two-component models fit the observed dPA distributions well, with all reduced χ^2 close to one and $0.16 < P_{\rm null} < 0.84$[6], which indicates a good fit and no over-fitting.

The simulation results show that the w of the bright&massive and faint&massive samples are significantly different. This confirms the conclusion based on the K-S test in Sect. 5.3.1 and implies that the jet alignment depends on the radio luminosity in our work. Radio AGNs with a lower luminosity have jets more likely to be aligned with the minor axis of the host galaxies.

We also selected the simulated sources with an apparent axis ratio

[6]The range of 0.16 to 0.84 corresponds to the 1-σ confidence interval in the Gaussian distribution.

Sample	w	$\chi^2/d.o.f$	$P_{\rm null}$
FinAGN	0.157 ± 0.026	0.89	0.51
Bright&massive	0.134 ± 0.054	1.39	0.204
Faint&massive	0.316 ± 0.062	1.08	0.37
Bright&round	0.006 ± 0.060	0.48	0.85
Bright&elongated	0.221 ± 0.051	1.17	0.32

Table 5.2: The best-fit results of the two-component fitting for different radio AGN samples. The goodness-of-fit can be implied from the null-probability $P_{\rm null}$, which quantifies the probability that the simulated distribution is similar to the observation.

of $q > 0.7$ and $q \leqslant 0.7$ as the simulated round and elongated sources. They were used to fit the bright&round and the bright&elongated samples defined in Sect. 5.3.2. The best-fit results are shown in Fig. 5.15 and Tab. 5.2. While the two-component model fits the bright&elongated sample well, the $P_{\rm null}$ result for the bright&round sample is larger than 0.84, indicating possible overfitting. This can also be implied from the w result, which is small and has a large error. The best-fit w for the bright&round sample implies that the jets in these radio AGNs are less likely to be aligned with the minor-axis of the host galaxies than those in the other samples. The non-overlapping confidence intervals of the best-fit w for the bright&round and bright&elongated suggested the flattened dPA distribution in the bright&round sample cannot be explained by the projection effect. Therefore, the jet alignment is also dependent on the shape of galaxies.

As the simulation results could depend on the intrinsic galaxy morphology model, i.e. T and E, we also tried to do the simulations with T and E 0.1 larger or smaller than the best-fit T, E. Although the projected axis ratio of these galaxy morphology models are significantly different from the observed distribution, the best fit w do not change significantly and most of the resulting w fall in the 1-σ ranges of the results using the best-fit galaxy morphology model, but with worse $P_{\rm null}$. Therefore, our results seem robust and not very sensitive to the galaxy morphology model.

5.5 Conclusions & Discussion

We have selected a radio AGN sample with reliable RPA and OPA measurements based on the LoTSS DR2 and FIRST data. We investigated the

alignment result between radio-AGN jets relative to their host galaxies by comparing optical and radio images of radio galaxies, followed by modelling intrinsic jet alignment to apparent jet alignment. Our conclusions are summarised as follows:

i In all the radio AGN samples, the dPA distributions indicate a minor-axis alignment, in contrast to the major-axis alignment distribution for the SF galaxies.

ii We divided the radio AGN sample into subsamples with different $L_{150\,\mathrm{MHz}}$ and $M_\star$. We found a possible upturn or flatten trend at small dPAs ($\lesssim 30^\circ$) in all subsamples except the bright&less massive subsample.

iii We found a significant projected dPA difference between the bright and faint radio AGNs in round galaxies. The faint radio AGNs tend to be more minor-axis aligned.

iv We used a single-component and a two-component model to simulate the observed dPA distributions. The dPA distributions are best described by the two-component models. The fitting results indicate that the jet alignment is dependent on radio luminosity and the shape of galaxies, with the jets being more likely to be aligned with the minor-axis of the galaxy for lower luminosity and elongated radio AGNs.

The implication of the conclusions is that most of SMBHs associated with these radio-AGN sources undertake a coherent model-dominated accretion process, as mentioned in Lagos et al. (2011). Conversely, for SMBHs of bright radio-AGN within massive host galaxies, their accretion processes can be related to the chaotic accretion or merger events (Lagos et al. 2011; Hopkins et al. 2012). Therefore their dPA distributions indicate that the radio-AGN jets are less aligned with the minor axis of the host galaxy. This scenario can also be implied from the less aligned dPA distribution for the round galaxies, which are more likely to have been through a major merger.

The minor-axis alignment between radio jets and their host galaxies in the radio AGN samples provides some important insights into the evolutionary history of galaxies. As indicated by previous studies (Simmons et al. 2017; Martin et al. 2018; Smethurst et al. 2019; McAlpine et al. 2020;

Smethurst et al. 2021), in general, SMBH growth is dominated by a secular process resulting from gas inflow in both merger-free and merger-frequent galaxies (Natarajan & Pringle 1998). An important feature of the secular growth of SMBHs at centres of galaxies is the production of radio-AGN jets aligned with their host galaxies' angular momentum (Beckmann et al. 2022). Our result that the majority of radio jets are roughly aligned with their galactic zenith, therefore, reinforced the aforementioned evidence. That is, the majority of galactic SMBHs grow via the coherent secular process between merger events, and associated SMBH spins result in radio-AGN jets mostly aligned toward their galactic zenith.

By contrast, for an extreme system, such as bright radio-AGN hosted by massive galaxies, radio-AGN jets might not be aligned towards their galactic zenith. The potential cause of the random orientations among these radio-AGN jets would be recent merger events. After a merger event, SMBH spins could be misaligned with respect to their host galaxies' angular momentum, and the spins might take time to realign under the Bardeen-Petterson effect (Bardeen & Petterson 1975). The timescale for this effect is thought to be much shorter compared to the secular process of SMBH growth (Natarajan & Pringle 1998). Hence, the misalignment is only observed in a small population of galaxies under extreme post-merger environments. This is also contributed by the fact that our sample consists of mostly gas-poor early-type galaxies. For these galaxies after recent merger events, achieving a stable accretion inflow is thought to be unlikely, and chaotic accretion is a reasonable scenario, which prolongs post-merger misalignments in SMBH jets (Bustamante & Springel 2019).

In addition, for the bright radio-AGN hosted by massive galaxies, we also speculated the reason for a possible secondary population below the alignment angle of 40°. One of the possible reasons for the secondary population is that the radio emission comes from the SF activities in their galactic planes. To further investigate the potential secondary population in the group of bright radio AGN with massive host galaxies, we separated this sub-sample into two different categories, for radio-AGN with alignment angles below 40° and for radio-AGN with alignment angles above 40°. The two categories of SFR distributions were subsequently compared. The SFR for two different populations share a similar trend, with the majority of the sources having their SFR $< 1\,M_{\odot}$ yr^{-1} (87.4% for alignment below 40° and 89.5% for alignment above 40°). The low SFRs indicate that the cause of the secondary population is not due to stellar

activities within corresponding sources' galactic planes, which is implied in Fig. 5.8.

Our results provide essential observational evidence for the simulation results in recent studies (e.g. Beckmann et al. 2022), especially regarding the alignment between SMBH spins and their host galaxies' angular momentum. Provided the evidence of coherent secular process-dominated SMBH growth in long-lasting epochs between merger events, additional evidence of the influence of radio-AGN outflows on their host galaxies might be crucial to further understand the overall co-evolution between galaxies and their central SMBHs.

Acknowledgements

XCZ acknowledges support from the CSC (China Scholarship Council)-Leiden University joint scholarship program.

LOFAR data products were provided by the LOFAR Surveys Key Science project (LSKSP; https://lofar-surveys.org/) and were derived from observations with the International LOFAR Telescope (ILT). LOFAR (van Haarlem et al. 2013) is the Low Frequency Array designed and constructed by ASTRON. It has observing, data processing, and data storage facilities in several countries, that are owned by various parties (each with their own funding sources), and that are collectively operated by the ILT foundation under a joint scientific policy. The efforts of the LSKSP have benefited from funding from the European Research Council, NOVA, NWO, CNRS-INSU, the SURF Co-operative, the UK Science and Technology Funding Council and the Jülich Supercomputing Centre.

This research uses services or data provided by the Astro Data Lab at NSF's National Optical-Infrared Astronomy Research Laboratory. NOIRLab is operated by the Association of Universities for Research in Astronomy (AURA), Inc. under a cooperative agreement with the National Science Foundation.

The Legacy Surveys consist of three individual and complementary projects: the Dark Energy Camera Legacy Survey (DECaLS; NOAO Proposal ID # 2014B-0404; PIs: David Schlegel and Arjun Dey), the Beijing-Arizona Sky Survey (BASS; NOAO Proposal ID # 2015A-0801; PIs: Zhou Xu and Xiaohui Fan), and the Mayall z-band Legacy Survey (MzLS; NOAO Proposal ID # 2016A-0453; PI: Arjun Dey). DECaLS, BASS and MzLS together include data obtained, respectively, at the Blanco telescope, Cerro Tololo Inter-American Observatory, NSF's National Optical Infrared Astronomy Research Laboratory (NOIRLab); the Bok telescope, Steward Observatory, University of Arizona; and the Mayall telescope, Kitt Peak National Observatory, NOIRLab. The Legacy Surveys project is honored to be permitted to conduct astronomical research on Iolkam Du' ag (Kitt Peak), a mountain with particular significance to the Tohono O' odham Nation.

The NSF's NOIRLab is operated by the Association of Universities for Research in Astronomy (AURA) under a cooperative agreement with the National Science Foundation. Database access and other data services are provided by the Astro Data Lab.

BASS is a key project of the Telescope Access Program (TAP), which has been funded by the National Astronomical Observatories of China, the Chinese Academy of Sciences (the Strategic Priority Research Program "The Emergence of Cosmological Structures" Grant # XDB09000000), and the Special Fund for Astronomy from the Ministry of Finance. The BASS is also supported by the External Cooperation Program of Chinese Academy of Sciences (Grant # 114A11KYSB20160057), and Chinese National Natural Science Foundation (Grant # 11433005).

The Legacy Surveys team makes use of data products from the Near-Earth Object Wide-field Infrared Survey Explorer (NEOWISE), which is a project of the Jet Propulsion Laboratory/California Institute of Technology. NEOWISE is funded by the National Aeronautics and Space Administration.

The Legacy Surveys imaging of the DESI footprint is supported by the Director, Office of Science, Office of High Energy Physics of the U.S. Department of Energy under Contract No. DE-AC02-05CH1123, by the National Energy Research Scientific Computing Center, a DOE Office of Science User Facility under the same contract; and by the U.S. National Science Foundation, Division of Astronomical Sciences under Contract No.AST-0950945 to NOAO.

This project used data obtained with the Dark Energy Camera (DECam), which was constructed by the Dark Energy Survey (DES) collaboration. Funding for the DES Projects has been provided by the U.S. Department of Energy, the U.S. National Science Foundation, the Ministry of Science and Education of Spain, the Science and Technology Facilities Council of the United Kingdom, the Higher Education Funding Council for England, the National Center for Supercomputing Applications at the University of Illinois at Urbana-Champaign, the Kavli Institute of Cosmological Physics at the University of Chicago, Center for Cosmology and Astro-Particle Physics at the Ohio State University, the Mitchell Institute for Fundamental Physics and Astronomy at Texas A&M University, Financiadora de Estudos e Projetos, Fundação Carlos Chagas Filho de Amparo, Financiadora de Estudos e Projetos, Fundação Carlos Chagas Filho de Amparo à Pesquisa do Estado do Rio de Janeiro, Conselho Nacional de Desenvolvimento Científico e Tecnológico and the Ministério da Ciência, Tecnologia e Inovação, the Deutsche Forschungsgemeinschaft and the Collaborating Institutions in the Dark Energy Survey. The Collaborating Institutions are Argonne National Laboratory, the University of California at Santa Cruz, the University of Cambridge, Centro de Investigaciones Enérgeticas, Medioambientales y Tecnológicas – Madrid, the University of Chicago, University College London, the DES-Brazil Consortium, the University of Edinburgh, the Eidgenössische Technische Hochschule (ETH) Zürich, Fermi National Accelerator Laboratory, the University of Illinois at

Urbana-Champaign, the Institut de Ciències de l'Espai (IEEC/CSIC), the Institut de Física d'Altes Energies, Lawrence Berkeley National Laboratory, the Ludwig-Maximilians Universität München and the associated Excellence Cluster Universe, the University of Michigan, the National Optical Astronomy Observatory, the University of Nottingham, the Ohio State University, the University of Pennsylvania, the University of Portsmouth, SLAC National Accelerator Laboratory, Stanford University, the University of Sussex, and Texas A&M University.